

Article

Microstructural Characteristics of Plasma Sprayed NiCrBSi Coatings and Their Wear and Corrosion Behaviors

Songqiang Huang ¹, Jingzhong Zhou ¹, Kuoteng Sun ¹, Hailiang Yang ¹, Weichen Cai ¹, Yi Liu ^{2,*}, Ping Zhou ², Shuangjie Wu ² and Hua Li ²

¹ Liuzhou Bureau, EHV Transmission Company, China Southern Power Grid Co., Ltd., Liuzhou 545006, China; huangsongqiang@ehv.csg.cn (S.H.); zhoujz@csg.cn (J.Z.); sunkuoteng@ehv.csg.cn (K.S.); yanghailiang@ehv.csg.cn (H.Y.); caiweichen@ehv.csg.cn (W.C.)

² Key Laboratory of Marine Materials and Related Technologies, Zhejiang Key Laboratory of Marine Materials and Protective Technologies, Ningbo Institute of Materials Technology and Engineering, Chinese Academy of Sciences, Ningbo 315201, China; zhouping@nimte.ac.cn (P.Z.); wushuangjie@nimte.ac.cn (S.W.); lihua@nimte.ac.cn (H.L.)

* Correspondence: liuyi@nimte.ac.cn; Tel.: +86-574-8668-6224; Fax: +86-574-8668-5159

Abstract: Nickel-based alloys are commonly used as protective coating materials for surface protection applications owing to their superior resistance to corrosion, wear and high-temperature oxidation. It is urgent to study the fundamental mechanism between the structure and corrosion properties of the Nickel-base composite coatings. This paper, therefore, focuses on clarifying the mechanisms of the microstructure influencing the acid corrosion and mechanical characteristics of the as-sprayed NiCrBSi coating and post-heat-treated coating. The formation mechanisms of the amorphous phase of flat particles during the plasma spray process were studied by using X-ray diffraction analysis, Raman spectroscopy and confocal laser scanning microscope at first. Then the evolutionary process of the corrosion structure and phase of the coating in the accelerated corrosion experiment is directly visualized by using scanning electron microscopy and energy spectrum analysis. The mechanical properties of the amorphous NiCrBSi coatings are lastly measured by microhardness and friction wear tests. The critical phenomena and results help to elucidate the relative influence of the surface features of atmospheric plasma sprayed coatings on acid corrosion responses and wear resistance, aiming at contributing to the development of a protective technique for electrical engineering.

Keywords: amorphous coating; plasma spray; heat treatment; corrosion; wear behavior



Citation: Huang, S.; Zhou, J.; Sun, K.; Yang, H.; Cai, W.; Liu, Y.; Zhou, P.; Wu, S.; Li, H. Microstructural Characteristics of Plasma Sprayed NiCrBSi Coatings and Their Wear and Corrosion Behaviors. *Coatings* **2021**, *11*, 170. <https://doi.org/10.3390/coatings11020170>

Academic Editor: Philipp Vladimirovich Kiryukhantsev-Korneev

Received: 12 January 2021

Accepted: 27 January 2021

Published: 31 January 2021

Publisher's Note: MDPI stays neutral with regard to jurisdictional claims in published maps and institutional affiliations.



Copyright: © 2021 by the authors. Licensee MDPI, Basel, Switzerland. This article is an open access article distributed under the terms and conditions of the Creative Commons Attribution (CC BY) license (<https://creativecommons.org/licenses/by/4.0/>).

1. Introduction

The continuous corrosion and erosion of power transmission and transformation facilities bring about a number of problems, including flashover accidents, broken wires or inverted towers, which causes huge economic losses and security risks every year. Thus, it is urgent to develop new materials and protective technology. Compared with crystalline alloys, amorphous alloys exhibit an unbalanced metastable state and disordered atomic arrangement, resulting in a higher system free energy. As a result of these characteristics, amorphous alloys possess high hardness and excellent wear and corrosion resistance [1–4].

Nickel-based alloys are commonly used as protective coating materials for industrial applications owing to their superior resistance to corrosion, wear and high-temperature oxidation [5–7]. Among different Ni-based alloy coatings, NiCrBSi is a self-fluxing alloy due to the presence of B and Si, which enhances the self-fluxing property of the metal which is favorable for coating deposition, and forms a hard phase with Ni, such as Ni₃B [8–10]. In addition, chromium can further improve its corrosion and wear resistance through the precipitation of hard particles. NiCrBSi alloys with good amorphous forming ability provide even higher mechanical strength, high corrosion and wear resistance, low stiffness

and good elasticity, which is widely used in engines, piston rods, and boilers because of their high resistance against wear and corrosion [11–13].

Up to now, NiCrBSi composite coating can be rapidly deposited by thermal spraying techniques, including atmospheric plasma spraying (APS), arc spray (AS), flame spraying (FS) or high-velocity oxygen fuel spraying (HVOFS) [14–17]. By using these techniques, the amorphous coatings are prepared by melting the feedstock particles into droplets, impinging the droplets onto a cold substrate and forming the coatings by rapid solidification in situ. Previous works have reported that NiCrBSi-based thermally sprayed coatings containing amorphous structures exhibit high hardness and wear-corrosion resistance [18,19]. Planche et al. compared the characteristics of the NiCrBSi coatings sprayed by using plasma, flame and HVOF processes [20]. It was found that plasma coating was completely amorphous because of the highest cooling rate and relatively low substrate temperature (about 160 °C). In comparison, the particles obtained the highest particle temperature and the highest particle velocity via flame spray and HVOF respectively, both of which lead to a certain portion of crystallized phase in the coating. Additionally, Serres et al. modified the structural characteristics of metallic NiCrBSi and composite NiCrBSi–WC coatings by using atmospheric plasma spray (APS) with a different content ratio of WC [21]. It was reported that the increase in the amorphous phase and better mechanical properties can be realized for higher WC content in the composite coating layer. Among different coating techniques, APS is simple, flexible, and low cost, which can generate a high flame temperature (>10,000 K) as well as ultra-high cooling speed (10^5 – 10^7 K/s). During the rapid melting and solidification process, numerous amorphous phases can be readily formed in as-sprayed coatings through the APS process [20,21].

However, unfortunately, fundamental understanding of amorphous NiCrBSi coating during plasma spraying falls far behind its practical applications. In this paper, we studied the formation mechanisms of the amorphous phase of flat particles during the plasma spray process, based on which the relationship between the wear and corrosion properties and the microstructure of the amorphous coatings are also clarified.

2. Materials and Methods

Commercially available NiCrBSi powder with an average size (D50) of about 70 μm was used for the coating deposition. The chemical composition of NiCrBSi powder was illustrated in Table 1, and the SEM figures were pictured in Figure 1a,b. To clarify the amorphous forming ability of the particles at particle/substrate interface and performance of the coating, polished 316 L stainless steel substrate with the size of 20 mm \times 30 mm \times 2 mm was used as the substrates for the coating deposition. Prior to the spraying, the substrates were cleaned by sonication in an acetone bath and dried at 120 °C.

Table 1. Chemical composition of NiCrBSi powders.

Element	Ni	Cr	B	Si	Fe	C
wt.%	61.2	15.5	3.5	4.0	15.0	0.8

The APS-2000K plasma spray system (Beijing Aeronautical Manufacturing Technology Research Institute, Beijing, China) was used to deposit the coatings. To attain the desired structure of the NiCrBSi coatings, plasma spray power and gun moving speed were optimized and the robot-controlled moving speed was set within the range of 300 mm/s. The spray distance was 120 mm and the plasma power was 30 kW, where the current and voltage was 500 A and 60 V, respectively. The feeding rate of feedstocks was 10 g/min. The diagram of the APS system was shown in Figure 1c.

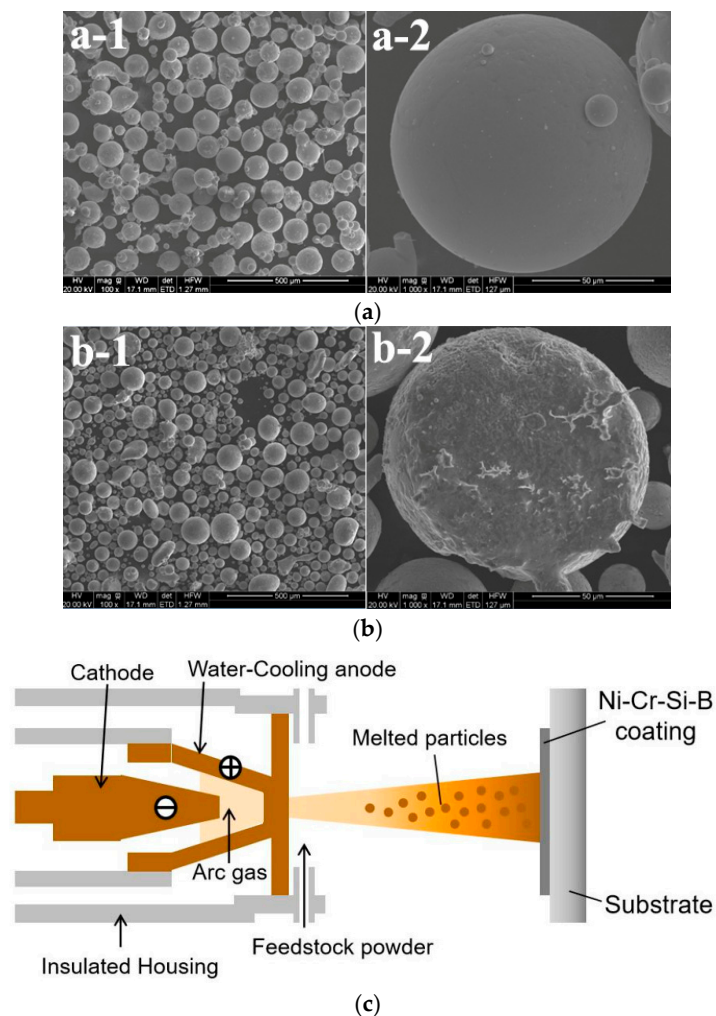


Figure 1. SEM images of (a) raw NiCrBSi powder and (b) plasma sprayed NiCrBSi powder. (a-1,b-1): low magnification, (a-2,b-2): high magnification. (c) Diagram of the APS (atmospheric plasma spray) system.

The microstructure of the powder and the coating samples was characterized by field emission scanning electron microscopy (FESEM, FEI Quanta FEG250, Eindhoven, The Netherlands) and confocal laser scanning microscope (CLSM: ZEISS, LSM700, Oberkochen, Germany). High-resolution transmission electron microscopy (HRTEM) was employed to characterize the structural evolution of the interfacial areas between coating and substrate or among individual impacted particles at a near-atomic-scale. The phase composition of the powders and coatings was detected by X-ray diffraction (XRD, Rigaku-D/max2400, Tokyo, Japan) with $\text{CuK}\alpha$ ($\lambda = 1.5405 \text{ \AA}$) radiation operating at 40 kV and 100 mA. The goniometer was set at a scan rate of $2^\circ/\text{min}$ over a 2θ range of $20\text{--}90^\circ$. The structure of the samples was further measured by a Raman spectrometer (Renishaw inVia Reflex, Renishaw, Wotton-under-Edge, UK) with a resolution of 8 cm^{-1} and a scan number of 4 at a spectral region ranging from 400 to 1850 cm^{-1} . In addition, to evaluate the crystallization behavior of NiCrBSi, differential scanning calorimetry testing (DSC, Pyris Diamond DSC, Perkin-Elmer, Waltham, MA, USA) was conducted for the samples. For the DSC test in a nitrogen atmosphere, the heating rate of the samples was $10 \text{ }^\circ\text{C}/\text{min}$. The DSC crystallization behavior of NiCrBSi coating was analyzed in Part 1 of the Supplementary Materials.

To examine the corrosion resistance of the NiCrBSi coatings, the surface morphology was studied after acid accelerated corrosion by using HF- HNO_3 solution. A mixture solution of HNO_3 :HF (analytical reagent) with a ratio of 3:1 was prepared by using a plastic beaker. Each sample (as sprayed and post heat treated) was corroded for 5 s by

pouring the prepared corrosion solution evenly on the surface of the sample, rinsed with plenty of water and alcohol by 5 min, respectively. After that, the samples were dried by using electric dryer and hot air. Lastly, the structural and morphological properties were examined and compared by using Raman spectrometer and FESEM.

To examine the mechanical properties of the NiCrBSi coatings, Vickers hardness of the coatings was measured on their polished cross sections using the microhardness tester (HV-1000, Shanghai Lianer Testing Equipment Corporation, Shanghai, China) with a load of 4.9 N and a duration of 10 s and ten points averaged for each sample. The tribological properties of the coatings were assessed by sliding wear test conducted on a reciprocating-type ball-on-disc tribometer (UMT-3, CETR, Waltham, MA, USA). The reciprocating frequency was 1 Hz. The tests were performed for 600 s at room temperature under a load of 15 N with an average sliding speed of 10 mm/s. As a typical type of bearing steel, GCr15 steel balls with the size of 3 mm in diameter were used as the counterparts. Prior to each test, the GCr15 balls were ultrasonically cleaned in acetone, and a new ball or a new position of the ball was adopted for each test. Five samples were tested for each type of the coatings. The friction coefficient as the function of sliding time was recorded during the test. After the test, wear loss in terms of wear mass was determined using a weighing method with sensitivity of 0.0001 g, and the wear rate was also calculated. Morphological features of the worn surfaces were observed by field emission scanning electron microscopy (FESEM, FEI Quanta FEG250).

3. Results and Discussion

As shown in Figure 2, the XRD patterns of the raw NiCrBSi powder, as-sprayed and heat treated NiCrBSi coatings are compared. It can be found that the coatings consist of the main phase of γ -Ni (JCPDS No. 45-1027) and Ni₃B (JCPDS No. 98-007-5794), and several kinds of trace phases, including Cr₇C₃ (JCPDS No. 11-0550) and M₂₃C₆ (JCPDS No. 35-0783). As to the trace phases, it was reported that the space groups of M₂₃C₆ and M₇C₃ are *Fm3m*(cubic) and *Pnma*(orthorhombic), respectively [22]. Here, M represents the metal elements including Ni or Cr. The plasma sprayed NiCrBSi coating exhibited a broad peak at 2θ from 40° to 50°, indicating the predominate presence of amorphous phase in the as-sprayed coating. It should be noted that the as-sprayed coating shows certain nanocrystalline phases around $2\theta \approx 52^\circ$ and 76° . During the plasma spraying process, the NiCrBSi feedstock are melted and then solidified between 10^{-8} and 10^{-6} s, which is measured by a DPV 2000 Diagnostic System (TECNAR Automation LTD., Saint-Bruno, Quebec, Canada). Therefore, large amounts of amorphous phase inevitably forms in the plasma sprayed NiCrBSi coating. Post heat treatment is usually helpful for obtaining a dense coating with high cohesion and adhesion strengths. The broad peak became sharper after heat treatment at 600 °C for 1 h, indicating that the recrystallization of the amorphous phase.

The morphology and Raman spectra of a flat amorphous NiCrBSi particle are studied. Firstly, the optical microscope photograph and 3D morphology of the particle are characterized, as shown in Figure 3(a-1,a-2), respectively. The reference is selected below the matrix and above the highest point of the particle to ensure that the whole particle is in the detection range. Pseudo color map is used to characterize the relative height of different regions of the particle, and the red curve across the flat particle shows a trend of height change in one direction. The color of the 3D structure diagram shows that the surrounding area of the flat particles is about 1 μm higher than that of the flat area in the center, and some protrusions are about 3 μm higher than the central area, which is caused by the incomplete flattening of the molten particles during the rapid cooling. When the curve reaches the boundary of the flat particles, it appears that the bottom surface of the particle is lower than the matrix, which may be caused by partial melting of the matrix or deformation caused by the force. The surface height of flat particles fluctuates, and the surface roughness R_a is 0.224 μm .

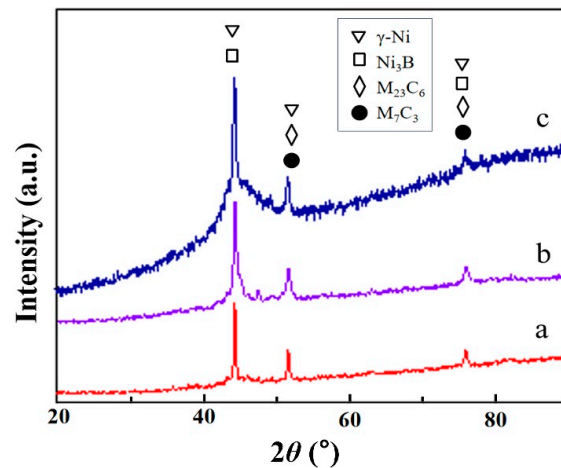


Figure 2. XRD patterns of (a) raw NiCrBSi powder, and (b) post heat-treated and (c) plasma sprayed NiCrBSi coating.

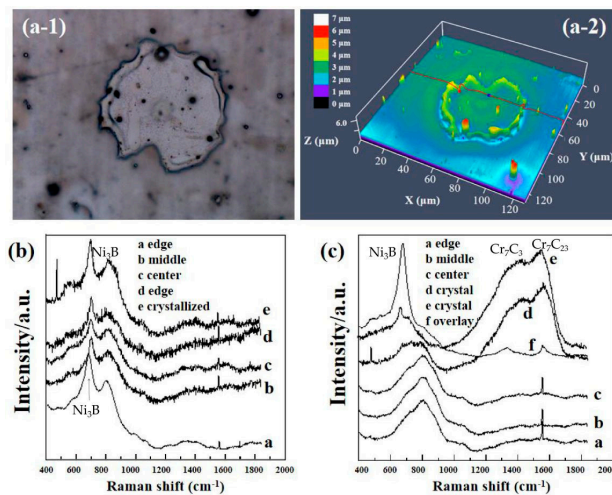


Figure 3. (a-1) Optical photographs and (a-2) CLSM images showing the surfaces of a deposited flat NiCrBSi particle, and phase composition of (b) a deposited flat NiCrBSi particle and (c) after corrosion process.

The Raman spectra of an as-sprayed flat particle are further characterized in Figure 3b. The curves a, b and c are corresponded to the edge, middle and center of a flat particle. As shown in Figure 3b, the peak positions of the curves locate at 670–700, 1325 and 1430 cm^{-1} . It should be noted that there is a minor deviation in the curve a in comparison to other curves, which is probably attributed to the manifestation of stress, indicating that the stress of the edge is different from the center when the particle is melted spreading. Comparing to the curve d, curve e exhibited a sharp peak at 473 cm^{-1} , which indicated the partial crystallization of certain region of the flat particle.

To make a comparison, the Raman spectra selected for a corroded particle are demonstrated in Figure 3c. The curves a, b, c are the Raman spectra at the edge, middle and center of the same particle, which are basically consistent with each other, indicating the structure of the corroded particle is uniform. A broadening peak at 809 cm^{-1} discloses the coexistence of amorphous and crystalline phases in this region, while the sharp peak at 1554 cm^{-1} indicates that it refers to a dominating crystallization phase. The curve d and e are selected from a crystallized region in the corroded particle, and the peaks appear at 473, 670–700, 1430 and 1554 cm^{-1} , where the 670–700 cm^{-1} peak corresponding to the

presence of Ni_3B [23]. The broadening peaks at 1430 and 1554 cm^{-1} prove the presence of a few amorphous phase. Additionally, the curve *f* represents an overlapped region of flat particles, where the relatively high intensity of the $670\text{--}700\text{ cm}^{-1}$ peak indicates that the region has a higher content of Ni_3B phase. The significant broadening peaks appeared at 1325 and 1554 cm^{-1} correspond to the amorphous phase of Cr_7C_3 and Cr_7C_{23} [24]. Raman analysis of the corroded flat particles shows that the structure is more complex, and the crystalline region still contains amorphous phase, while the overlapped particles are also a mixture of amorphous and crystallization phases.

A typical surface morphological diagram and the enlarged view of NiCrBSi coating are shown in Figure 4(a-1,a-2), respectively. It can be seen that the APS sprayed coating is quite well spread, where molten or semi-melted particles compacted the substrate after spreading and solidification processes to form a lamellar structured coating. Figure 4(b-1,b-2) further disclose the surface morphology after acid accelerated corrosion by using HF-HNO₃ solution. There are some unmelted spherical particles with the size of $\sim 50\text{ }\mu\text{m}$ in the coating. Additionally, partial flat particles form crystallized regions after deposition on the substrate. Both of which are prone to be corroded alongside the grain boundaries, resulting in textured surface composed of nano-crystallines, as shown in Figure 4(b-2). To be concluded, part of the uncorroded, smooth surface without fine grains distribution coexisted with the corroded, nano-crystallized region, where the smooth regions resistant to the acid are generally believed to contain higher amorphous content (See Part 2 of Supplementary Materials).

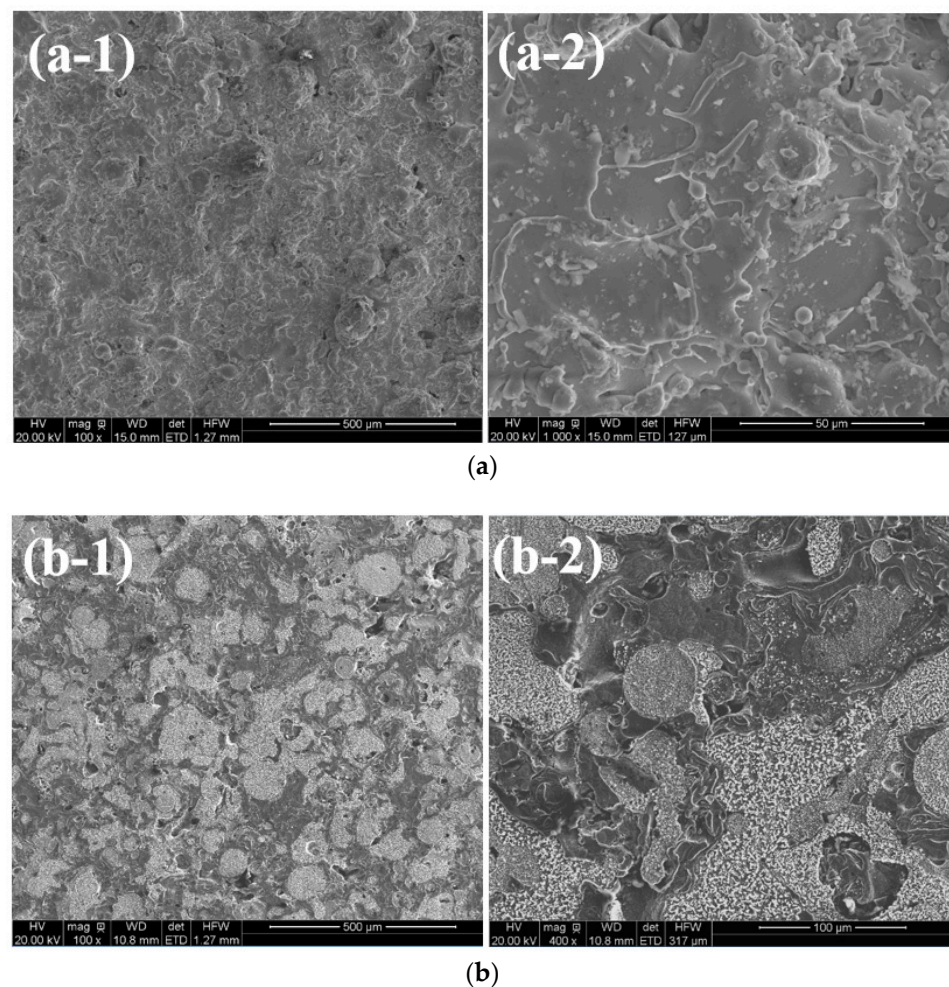


Figure 4. Typical surface view of (a) plasma sprayed NiCrBSi coating and (b) acid corrosion of plasma sprayed NiCrBSi coating. (a-1,b-1): low magnification, (a-2,b-2): high magnification.

To further disclose the anti-corrosion performance of the amorphous coating, the surface morphology of a lamellar splat after the strong acid accelerated corrosion experiment is further analyzed. Figure 5a presents the typical top view of the corroded particles with obviously fine grains. At the back-scattering imaging mode, two distinguished kinds of grains can be found in Figure 5b. When further enlarged, Figure 5c presents near-spherical shape grains with grain size less than $1\ \mu\text{m}$, which could be chromium carbide Cr_7C_3 and Cr_{23}C_6 by energy spectrum analysis (See Part 3 of Supplementary Materials). The relatively larger “fish bone-like” or “leaf-like” grains appear in Figure 5d, which can be mostly the Ni_3B phase, according to the analysis of energy spectrum results (See Part 4 of Supplementary Materials). Where the Cr content increases and Ni content decreases significantly, according to the energy spectrum analysis.

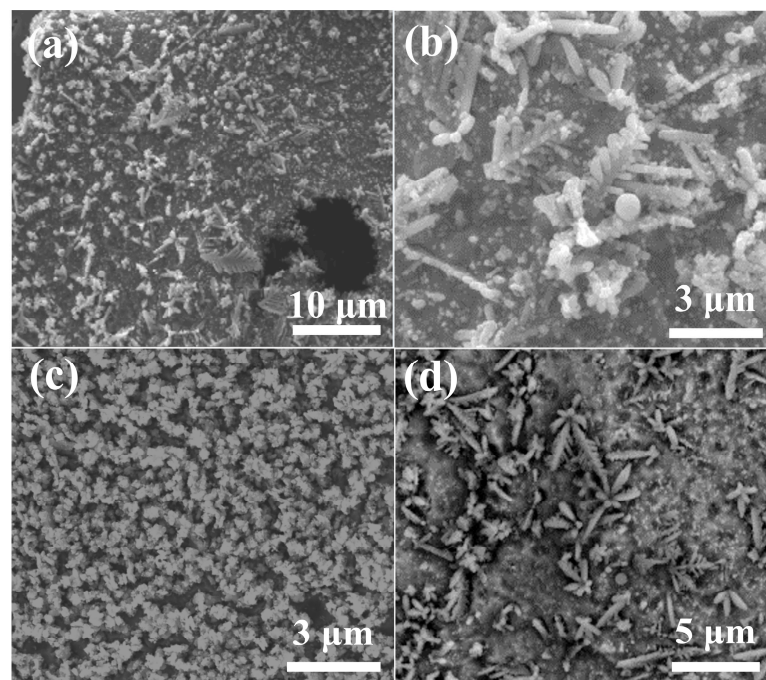


Figure 5. The surface morphology of a deposited flat NiCrBSi particle after acid corrosion. (a) low magnification image, (b) image at the back-scattering imaging mode, (c) near-spherical shape grains, and (d) “fish bone-like” or “leaf-like” grains.

Figure 6a shows the typical cross-sectional morphology of plasma sprayed NiCrBSi coating. As can be seen in Figure 6a, the uniform coating thickness is about $120\ \mu\text{m}$ and bonded well with the substrate. There is no apparent void or crack in the coating structure. However, there are a small number of interfaces distributed on the cross section, which is formed up by the piled flat particles. Figure 6b showed the cross-section image of NiCrBSi coating after polishing and subsequent HNO_3 -HF corrosion, where the coating is obviously lamellar structure, due to the accumulation of the sprayed flat particles, which is deposited by many passes to meet the requirements of coating thickness. Melted or semi-melted particles constantly impact on the substrate to spread out through the flow, then deformate into flat particles and form a layered coating.

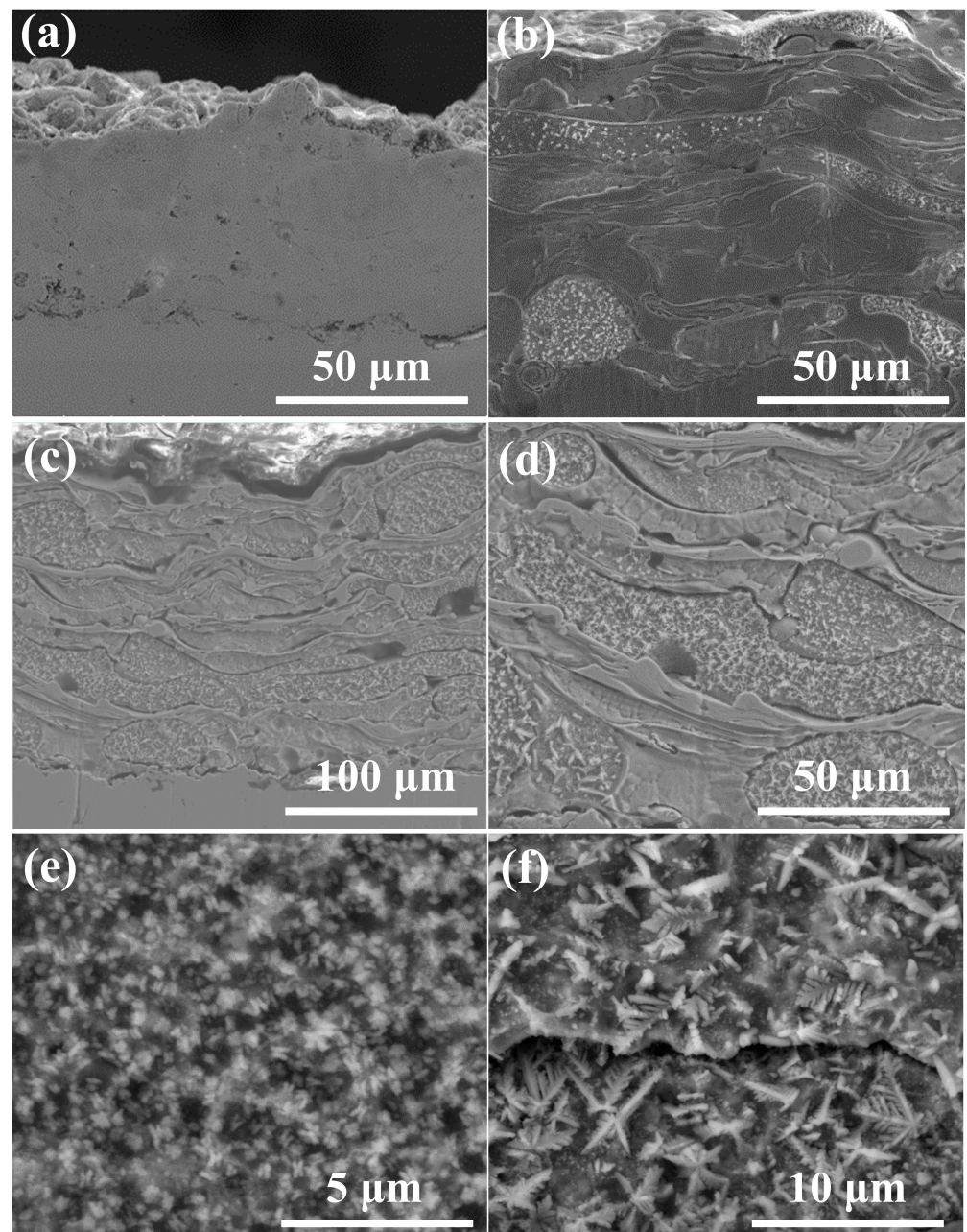


Figure 6. The cross section views of NiCrBSi coating and retained phases after acid accelerated corrosion. (a) Cross-sectional morphology of as-sprayed NiCrBSi coating, (b) after corrosion for 30 min, (c) after corrosion for 24 h, (d) high magnification of (c), (e) nano-sized grain region after corrosion for 24 h, and (f) “fish-bone like” or “leaf-like” grain region after corrosion for 24 h.

After corrosion, it can be seen that most of the region is smooth, indicating high amorphous content. However, there is also some spherical regions, which could be semi-melted or unmelted feedstocks not having enough driving force for amorphous formation. These hard particles are uniformly distributed in the amorphous coatings and can be corroded preferentially. Figure 6c,d reveal the cross-sectional morphology of the NiCrBSi coating after long time and severe corrosion. The microstructure of the coating can be clearly observed from the experimental results. The grains in the coating are mainly composed of about 200 nm grains and 3–8 μm “fish-bone like” or “leaf-like” grains shown in Figure 6e,f, respectively, which are identical to those in Figure 5b–d. The different phase components are caused by varied local aggregation states.

Hardness is one of the most important mechanical properties which directly determine the service performance and lifetime of the protective materials. Generally, the greater the hardness of the material is, the higher its wear resistance is. The microhardness analysis of the coating cross-section is used to analyze the mechanical properties corresponding to the microstructure distribution in the coating. During the spraying process, due to the differences in the spraying state, there are distinct differences in the composition, structure, size and quantity of pores, and the content of oxides. Hence, the as-sprayed coating is subjected to post treatment at 600 °C for 1 h, and the hardness test is carried out along the coating surface to the inside of the substrate.

The microhardness test results of as-sprayed NiCrBSi coating and post heat-treated coating are illustrated in Figure 7a. For the plasma sprayed NiCrBSi coating, from the coating-substrate interface to the coating surface, the microhardness gradually increases before it reached the maximum value of HV_{0.5} 640 near the coating surface, which is 2.4 times that of the stainless steel, suggesting good hardness of the amorphous coating.

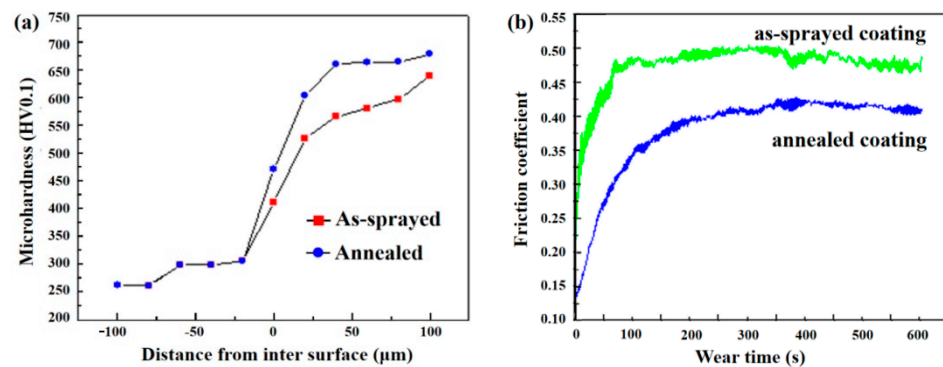


Figure 7. (a) Hardness and (b) friction coefficient of plasma sprayed NiCrBSi coating and post heat-treated NiCrBSi coating.

For the post heat-treated NiCrBSi coating at 600 °C, the microhardness of the coating gradually increases from the coating-substrate interface until the maximum value of HV_{0.5} 680 is reached near the coating surface. The microhardness of the heat treatment coating is higher than that of the as sprayed coating, suggesting the microhardness of the coating is obviously improved after crystallization treatment, which could be attributed to hard phases such as Cr₃C₇ precipitated during crystallization, which further promotes the increase in the coating hardness. At the same time, it can also be found that the hardness distribution of the as sprayed coating varies slightly during the test, while the hardness of the coating after heat treatment tends to be more stable, which shows that the microstructure after the heat treatment is relatively more uniform than that of the as sprayed coating.

The relationship between crystallization temperature and hardness of amorphous coatings has been reported in numerous literatures. For the crystallization treatment of the amorphous coating, the hardness will initially increase with the increase of temperature due to the crystallization of the amorphous phase. Then, the hardness will reach the maximum when the amorphous phase is fully crystallized. However, the hardness of the coating begins to decrease with further heat treatment due to the growth of the nanocrystals. It has been reported that the interfacial energy of amorphous-crystal is lower than that of the crystal-crystal interface. This composite structure inhibits the propagation of shear bands and cracks. It has also been reported that the superior mechanical properties of amorphous alloys or amorphous-nanocrystalline composites are related to the solute content of amorphous phase. The increase of nanocrystalline hardness is more affected by the solid solution strengthening of the remaining amorphous matrix than the nanoparticles themselves.

A Friction wear test is a test method to measure the wear resistance of plasma sprayed NiCrBSi coating. The reciprocating ball-disc friction wear tester (UMT-3, CETR, MA, USA) is used to evaluate the friction and wear properties of the coating. GCr15 steel balls with the diameter of 3 mm are used as the friction pair. The average sliding speed under 15 N load is 10 mm/s. The test time is 10 min. The reciprocating frequency is 1 Hz. The total sliding distance is 6 m. The measured temperature is 20 °C and humidity is 70%. Figure 7b shows the comparison of the friction coefficient results between the sprayed and heat-treated coatings. The friction coefficient of the sprayed coating gradually became stable from 60 s, and finally stabilized at about 0.45. The friction coefficient of the crystallized coating is only stable after 250 s, and finally stable at about 0.38. The friction coefficient of the spray coating is higher than that of the heat-treated coating, which is due to the uneven microstructure and high surface roughness of the spray coating. Because of the above reasons, the friction coefficient has also been fluctuating greatly, which is unfavorable to the wear resistance of the material. The coating treated by crystallization is relatively uniform in microstructure, so the friction coefficient fluctuates less.

To further reveal the wear mechanism of the amorphous coating, the surface morphology of the sprayed coating and the crystallized coating is examined. Figure 8(a-1,a-2) present the surface morphology of the wear marks of the as sprayed coating. As can be seen from Figure 8(a-1), the worn surface is relatively smooth with a small number of cracks, where an approximately circular shape on the left is a flat particle. After the friction and wear test, cracks expanded from the boundary of the flat particle, probably due to the voids in the gap where the flat particles overlap each other. Nickel-based amorphous coating is a typical brittle material with a large number of raised particles on the surface, so the friction force and compressive stress will cause cracks in the defects below the oxide layer during wear. The boundaries of flat particles have high oxide content and are prone to wear and exfoliation. Figure 8(a-2) shows the fragmentation of as-deposited particle after friction and wear test. The reciprocating movement of the grinding ball causes fatigue damage to the surface structure of the coating, and the periodic movement reaches a certain degree, and the fatigue damage accumulating at the defect produces fatigue cracks. Under the action of periodic tangential force, the fatigue crack extends and causes the bulk to peel off. The presence of multiple cracks in the middle and surrounding areas of a single particle also indicates that the particles with poor flattening or poor melting exist independently in the coating, which is a high incidence area. Additionally, Figure 8(b-1,b-2) show the surface morphology of the wear marks after crystallization treatment. In Figure 8(b-1), a large number of fine debris can be seen sticking to the surface of the coating, which indicates that unlike the wear mechanism of amorphous material, the wear mechanism of nanocrystals is mainly attributed to adhesive wear. A large amount of debris continuously adhered to the coating surface can lead to a high wear rate. Figure 8(b-2) shows a crack between two incompletely melted particles, which may also be caused by pores and oxides, which is similar to that of the sprayed coating.

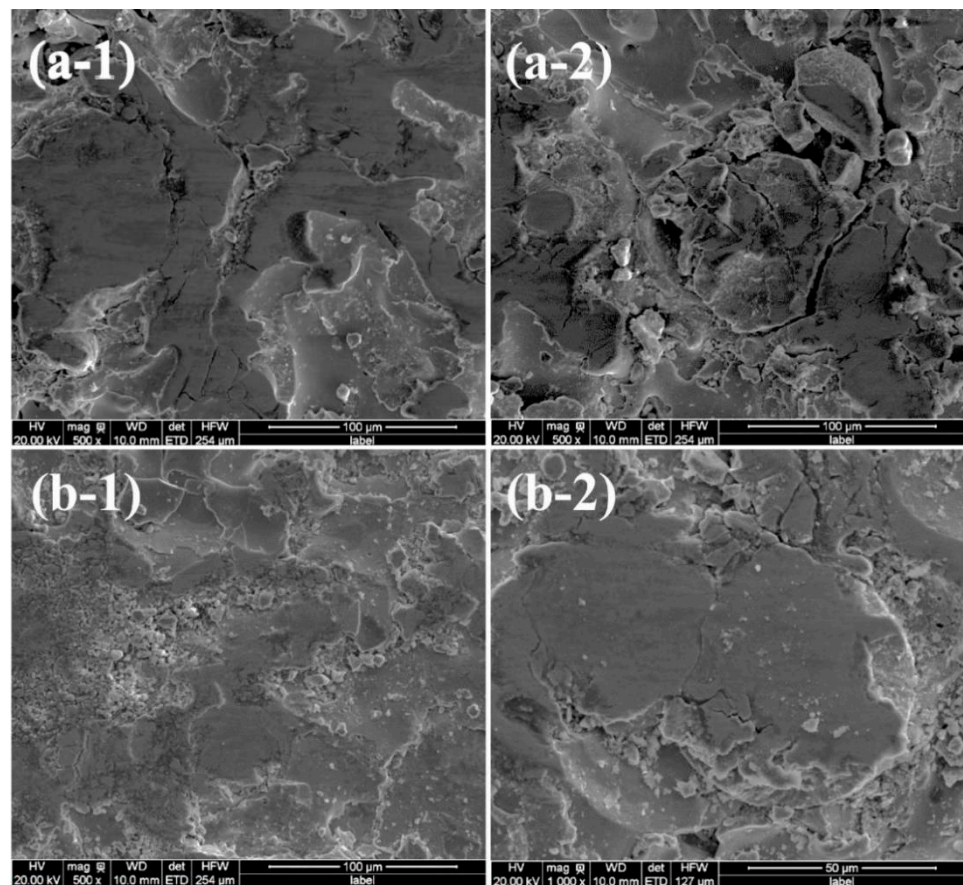


Figure 8. Surface morphology of (a-1,a-2) plasma sprayed NiCrBSi coating and (b-1,b-2) post heat-treated NiCrBSi coating before and after friction and wear test.

4. Conclusions

The NiCrBSi composite coating is successfully prepared by plasma spraying. The as-sprayed coating showed certain amorphous phase and nanocrystalline phases. The grains in the NiCrBSi coating are mainly composed of about 200 nm grains and 3–8 μm “fish-bone like” or “leaf-like” grains, which remained after accelerated acid corrosion tests by using HF:HNO₃ corrosive solution. The different phase components present local aggregation states. The microstructure is composed of Cr₇C₃, M₇C₂₃ and Ni₃B based on the XRD, SEM and Raman analysis. The microstructure homogenization of amorphous coating after the heat treatment is beneficial to promote the friction and wear characteristics. The microhardness of NiCrBSi coating gradually increases to the maximum value of HV_{0.5} 640 near the coating surface, which is 2.4 times that of the stainless steel. The maximum HV_{0.5} value is enhanced to 680 after post heat treatment, and the friction coefficient is reduced from about 0.45 to 0.38. This work gave some insights into the design and fabrication of protective coatings with controllable acid corrosion and mechanical properties for electrical engineering applications.

Supplementary Materials: The following are available online at <https://www.mdpi.com/2079-6412/11/2/170/s1>, Figure S1: Micro surface morphology of NiCrBSi coating, Figure S2: The SEM graph of the corroded flat particle with near-spherical shape grains, Figure S3: The SEM graph of the corroded flat particle with “fish bone-like” or “leaf-like” grains, Table S1: Elemental composition of the smooth area of NiCrBSi coating, Table S2: Elemental composition of the corroded flat particle with near-spherical shape grains, Table S3: Elemental composition of the corroded flat particle with “fish bone-like” or “leaf-like” grains.

Author Contributions: Experimental design and writing works, S.H.; Surface morphology of the samples, J.Z.; Characterization of the components and micro structures of the materials, K.S.; Corrosion experiments and analysis, H.Y.; Raman measurement and analysis, W.C.; Conception and experimental analysis, Y.L.; Air plasma spray coating of the samples, P.Z.; Wear property of the samples, S.W.; Polish and Finalization of the paper, H.L. All authors have read and agreed to the published version of the manuscript.

Funding: This research was supported by Technological Project of China Southern Power Grid Co., LTD “Research project on classification, operation and maintenance strategy of typical metal corrosion of transmission lines in Kunliulong DC transmission Project”, and National Natural Science Foundation of China (Grant # 52071329 and 51961015).

Institutional Review Board Statement: Not applicable.

Informed Consent Statement: Not applicable.

Data Availability Statement: Not applicable.

Conflicts of Interest: The authors declare no conflict of interest.

References

1. Jiang, C.; Liu, W.; Wang, G.; Chen, Y.; Xing, Y.; Zhang, C.; Dargusch, M. The corrosion behaviours of plasma-sprayed Fe-based amorphous coatings. *Surf. Eng.* **2017**, *34*, 634–639. [[CrossRef](#)]
2. Ghaziof, S.; Raeissi, K.; Golozar, M.A. Improving the corrosion performance of Cr–C amorphous coatings on steel substrate by modifying the steel surface preparation. *Surf. Coat. Technol.* **2010**, *205*, 2174–2183. [[CrossRef](#)]
3. Bacha, N.-E. Characterization of amorphous plasma sprayed coatings of FeCrPC and NiCrBSi. *J. Metastable Nanocrystalline Mater.* **2003**, *18*, 1–8. [[CrossRef](#)]
4. Li, C.-J.; Wang, Y.-Y.; Li, H. Effect of nano-crystallization of high velocity oxy-fuel-sprayed amorphous NiCrBSi alloy on properties of the coatings. *J. Vac. Sci. Technol. A* **2004**, *22*, 2000–2004. [[CrossRef](#)]
5. Liu, L.; Xu, H.; Xiao, J.; Wei, X.; Zhang, G.; Zhang, C. Effect of heat treatment on structure and property evolutions of atmospheric plasma sprayed NiCrBSi coatings. *Surf. Coat. Technol.* **2017**, *325*, 548–554. [[CrossRef](#)]
6. Chen, L.-Y.; Xu, T.; Lu, S.; Wang, Z.-X.; Chen, S.; Zhang, L.-C. Improved hardness and wear resistance of plasma sprayed nanostructured NiCrBSi coating via short-time heat treatment. *Surf. Coat. Technol.* **2018**, *350*, 436–444. [[CrossRef](#)]
7. Chen, L.-Y.; Wang, H.; Zhao, C.; Lu, S.; Wang, Z.-X.; Sha, J.; Chen, S.; Zhang, L.-C. Automatic remelting and enhanced mechanical performance of a plasma sprayed NiCrBSi coating. *Surf. Coat. Technol.* **2019**, *369*, 31–43. [[CrossRef](#)]
8. Shieh, Y.-H.; Wang, J.-T.; Shih, H.C.; Wu, S.-T. Allowing and post-heat treatment of thermal sprayed coatings of self-fluxing alloys. *Surf. Coat. Technol.* **1993**, *58*, 73–78. [[CrossRef](#)]
9. Cha, S.C.; Gudenau, H.W.; Bayer, G.T. Comparison of corrosion behaviour of thermal sprayed and diffusion-coated materials. *Mater. Corros.* **2002**, *53*, 195–205. [[CrossRef](#)]
10. Mahesh, C. Multiscale abinitio simulation of Ni-based alloys: Real-space distribution of atoms in $\gamma + \gamma'$ phase. *Comp. Mater. Sci.* **2015**, *108*, 192–204.
11. Gagandeep, S.; Manpreet, K.; Rohit, U. Wear and friction behavior of NiCrBSi coatings at elevated temperatures. *J. Therm. Spray Technol.* **2019**, *28*, 1081–1102.
12. Afsous, M.; Shafyeyi, A.; Soltani, M.; Eskandari, A. Characterization and evaluation of tribological properties of NiCrBSi–Gr composite coatings deposited on stainless steel 420 by HVOF. *J. Therm. Spray Technol.* **2020**, *29*, 773–788. [[CrossRef](#)]
13. Tang, L.; Kang, J.; He, P.-F.; Ding, S.-Y.; Chen, S.-Y.; Liu, M.; Xiong, Y.-C.; Ma, G.Z.; Wang, H. Effects of spraying conditions on the microstructure and properties of NiCrBSi coatings prepared by internal rotating plasma spraying. *Surf. Coat. Technol.* **2019**, *374*, 625–633. [[CrossRef](#)]
14. Rachidi, R.; El Kihel, B.; Delaunois, F. Microstructure and mechanical characterization of NiCrBSi alloy and NiCrBSi–WC composite coatings produced by flame spraying. *Mater. Sci. Eng. B* **2019**, *241*, 13–21. [[CrossRef](#)]
15. Wang, Y.; Stella, J.; Darut, G.; Poirier, T.; Liao, H.L.; Planche, M.P. APS prepared NiCrBSi–YSZ composite coatings for protection against cavitation erosion. *J. Alloys Compd.* **2017**, *699*, 1095–1103. [[CrossRef](#)]
16. Serres, N.; Hlawka, F.; Costil, S.; Langlade, C.; Machi, F. Microstructures of metallic NiCrBSi coatings manufactured via hybrid plasma spray and in situ laser remelting process. *J. Therm. Spray Technol.* **2010**, *20*, 336–343. [[CrossRef](#)]
17. Xiao, J.K.; Wu, Y.-Q.; Zhang, W.; Chen, J.; Wei, X.L.; Zhang, C. Microstructure, wear and corrosion behaviors of plasma sprayed NiCrBSi–Zr coating. *Surf. Coat. Technol.* **2019**, *360*, 172180. [[CrossRef](#)]
18. Guo, H.; Li, B.; Lu, C.; Zhou, Q.; Jia, J. Effect of WC–Co content on the microstructure and properties of NiCrBSi composite coatings fabricated by supersonic plasma spraying. *J. Alloys Compd.* **2019**, *789*, 966–975. [[CrossRef](#)]
19. Parthasarathi, N.L.; Duraiselvam, M. Improvement of high temperature wear resistance of AISI 316 ASS through NiCrBSiCFe plasma spray coating. *J. Miner. Mater. Charact. Eng.* **2010**, *9*, 653–670. [[CrossRef](#)]

20. Planche, M.P.; Liao, H.; Normand, B.; Coddet, C. Relationships between NiCrBSi particle characteristics and corresponding coating properties using different thermal spraying processes. *Surf. Coat. Technol.* **2005**, *200*, 2465–2473. [[CrossRef](#)]
21. Serres, N.; Hlawka, F.; Costil, S.; Langlade, C.; Machi, F. Microstructures and mechanical properties of metallic NiCrBSi and composite NiCrBSi-WC layers manufactured via hybrid plasma/laser process. *Appl. Surf. Sci.* **2011**, *257*, 5132–5137. [[CrossRef](#)]
22. Gorunov, A.I. Investigation of M_7C_3 , $M_{23}C_6$ and M_3C carbides synthesized on austenitic stainless steel and carbon fibers using laser metal deposition. *Surf. Coat. Technol.* **2020**, *401*, 126294. [[CrossRef](#)]
23. Heere, M.; Zavorotynska, O.; Deledda, S.; Sørby, M.H.; Book, D.; Steriotis, T.; Hauback, B.C. Effect of additives, ball milling and isotopic exchange in porous magnesium borohydride. *RSC Adv.* **2018**, *8*, 27645–27653. [[CrossRef](#)]
24. Fayer, A.; Glozman, O.; Hoffman, A. Deposition of continuous and well adhering diamond films on steel. *Appl. Phys. Lett.* **1995**, *67*, 2299–2301. [[CrossRef](#)]